

# Deep learning achieves radiologist-level performance of tumor segmentation in breast MRI

Lukas Hirsch, MS<sup>1\*</sup>, Yu Huang, PhD<sup>1,2\*</sup>, Shaojun Luo, PhD<sup>6</sup>, Carolina Rossi Saccarelli, MD<sup>2</sup>, Roberto Lo Gullo, MD<sup>2</sup>, Isaac Daimiel Naranjo, MD<sup>2</sup>, Almir G.V. Bitencourt, PhD<sup>2,7</sup>, Natsuko Onishi, MD, PhD<sup>2,3</sup>, Eun Sook Ko, PhD<sup>2,4</sup>, Dortis Leithner, MD<sup>2</sup>, Daly Avendano, MD<sup>2,5</sup>, Sarah Eskreis-Winkler, MD, PhD<sup>2</sup>, Mary Hughes, MD<sup>2</sup>, Danny F. Martinez, MS<sup>2</sup>, Katja Pinker, MD, PhD<sup>2</sup>, Krishna Juluru, MD<sup>2</sup>, Amin E. El-Rowmeim, MS<sup>2</sup>, MA<sup>2</sup>, Pierre Elnajjar, MS<sup>2</sup>, Hedvig Hricak, MD<sup>2</sup>, Elizabeth A. Morris, MD<sup>2</sup>, Hernan A. Makse, PhD<sup>6</sup>, Lucas C Parra, PhD<sup>1+</sup>, Elizabeth J. Sutton, MD<sup>2</sup>

1 Department of Biomedical Engineering, the City College of the City University of New York, New York, NY 10031

2 Department of Radiology, Memorial Sloan Kettering Cancer Center, New York, NY 10065

3 Department of Radiology, University of California, San Francisco, CA 94115

4 Department of Radiology, Samsung Medical Center, Sungkyunkwan University School of Medicine, Seoul, Korea

5 Department of Breast Imaging, Breast Cancer Center TecSalud, ITESM Monterrey, Monterrey, Nuevo Leon, Mexico.

6 Levich Institute and Department of Physics, the City College of the City University of New York, New York, NY 10031

7 Department of Imaging, A.C.Camargo Cancer Center, São Paulo, Brasil

\* first authors contributed equally  
+ corresponding author

**Funding Information:** Support for this work was provided in part by the National Institute of Health (NIH), National Science Foundation (NSF) through the following grants: NIH P30 CA008748; NIH R01EB022720, NIH R01MH111896; NIH R01EB022720, NSF DRL-1660548, as well as from the Breast Cancer Research Foundation and the Spanish Foundation Alfonso Martin Escudero.

**Originating Institution:** Memorial Sloan Kettering Cancer Center, 1275 York Avenue, New York, NY 10065

**Corresponding Author:** Lucas C Parra, Ph.D, The City College of New York, 160 Convent Avenue, New York, NY 10031

**Senior Author:** Elizabeth Sutton, MD, Memorial Sloan Kettering Cancer Center, 1275 York

Avenue, New York, NY 10065

### Abbreviations (no more than 10):

MRI = magnetic resonance imaging, TOST = two one-sided test, 2D/3D = two-dimensional/three-dimensional, BPE = background parenchymal enhancement, BIRADS = breast imaging reporting and data system, TPM = tissue probability map, CRF = conditional random field, T1c = post-contrast T1, DICOM = Digital Imaging and Communications in Medicine, ROC = receiver operating characteristic

### Key Points:

- We developed state-of-the-art deep convolutional networks to perform fully automated segmentation of malignant lesions in breast MRI using a large dataset consisting of 2,555 segmented malignant breasts and 60,108 benign breasts.
- The best performing network, a 3D U-Net operating on MRI contrast enhancement dynamic, achieves radiologist-level performance on an independent test set of 250 breasts with a Dice score of 0.77 and radiologist performance of 0.69-0.84.
- We make the code and pretrained network freely available to facilitate future studies on volumetric evaluation of malignant lesions.

## Abstract

**Purpose:** The goal of this research was to develop a deep network architecture that achieves fully-automated radiologist-level segmentation of breast tumors in MRI.

**Materials and Methods:** We leveraged 38,229 clinical MRI breast exams collected retrospectively from women aged 12-94 (mean age 54) who presented between 2002 and 2014 at a single clinical site. The training set for the network consisted of 2,555 malignant breasts that were segmented in 2D by experienced radiologists, as well as 60,108 benign breasts that served as negative controls. The test set consisted of 250 exams with tumors segmented independently by four radiologists. We selected among several 3D deep convolutional neural network architectures, input modalities and harmonization methods. The outcome measure was the Dice score for 2D segmentation, and was compared between the network and radiologists using the Wilcoxon signed-rank test and the TOST procedure.

**Results:** The best-performing network on the training set was a volumetric U-Net with contrast enhancement dynamic as input and with intensity normalized for each exam. In the test set the median Dice score of this network was 0.77. The performance of the network was equivalent to that of the radiologists (TOST procedure with radiologist performance of 0.69-0.84 as equivalence bounds:  $p = 5e-10$  and  $p = 2e-5$ , respectively;  $N = 250$ ) and compares favorably with published state of the art (0.6-0.77).

**Conclusion:** When trained on a dataset of over 60 thousand breasts, a volumetric U-Net performs as well as expert radiologists at segmenting malignant breast lesions in MRI.

## Introduction

Segmentation of breast tumors provides image features such as shape, morphology, texture, and enhancement dynamics that can improve diagnosis and prognosis in breast cancer patients (1–4). Reliable automated tumor segmentation does not yet exist, and manual segmentation is labor-intensive; this has precluded routine clinical evaluation of tumor volume despite mounting evidence that it is a good predictor of patient survival (3). Automatic segmentation with modern deep network techniques has the potential to meet this clinical need. Deep learning methods have been applied in breast tumor segmentation (5,6) and diagnosis (7–12) in mammograms, where large datasets of up to one million images are available, which greatly boosts the performance of the machine-learning systems (13,14). Yet unlike MRI, mammograms cannot determine the exact 3D location and volumetric extent of a lesion. Breast MRI has higher diagnostic accuracy than mammography (15–17) and outperforms mammograms in detecting residual tumors after neoadjuvant therapy (18). Additionally, background parenchymal enhancement (BPE) measured in MRI with dynamic contrast enhancement is predictive of cancer risk (19). Several studies have automated tumor segmentation in breast MRI using modern deep learning techniques such as U-Nets or DeepMedic (20–26). Unfortunately, the available MRI datasets have remained comparatively small (~300 cases or less); therefore, performance has been limited, with Dice scores in the range of 0.60–0.77. At present, trained radiologists outperform automated methods on MRI segmentation (21). We hypothesize that human-level performance can be achieved if a sufficiently large dataset is used to train a modern deep convolutional network. The goal of this research was to develop a deep-network architecture that achieves fully-automated radiologist-level segmentation of breast tumors in MRI by leveraging a dataset of over 60 thousand breast MRIs.

## Materials and Methods

### Study Design

We retrospectively accessed 38,229 clinical MRI breast exams performed for high-risk screening or diagnosis between 2002–2014, and partitioned them into training and test data at random (see Fig. 1, Table S1).

Segmentation was implemented in a deep network as a binary classification of every voxel in the MRI volume. To train the network, tumor voxels (classified as positive) were taken from 2D segmentations performed by dedicated breast radiologists. Negative examples were voxels taken from a central MRI slice of healthy breasts. Therefore, the network was trained to distinguish malignant from benign voxels, possibly including voxels in benign lesions.

Using the training data, we first selected the best performing network architecture, established the utility of the available imaging sequences, and selected an effective harmonization procedure.

We then compared the segmentations produced by the final network to those produced by trained radiologists in a separate test set of malignant cases segmented independently by four radiologists in 2D. Benign exams were not included in this analysis. The goal of this analysis was to determine if the performance of the network is equivalent to the performance of breast radiologists.

### Human Subjects

This study was approved by the Institutional Review Board and written informed consent was waived due to the retrospective nature of this study. All data handling complied with HIPAA regulations.

The patient population included 11,929 women who were enrolled in a screening program following established guidelines (27) and 2,546 women who were referred for diagnostic workup. The age range of the patient population was 12–94 years (mean age 52 years). The data included 3,955 breasts with biopsy-confirmed malignant tumors as well 60,108 breasts with benign pathology, defined here as BIRADS 1, 2, and 3 with two-year tumor-free follow-up. The types of tumors included in the study are listed in Fig. S1.

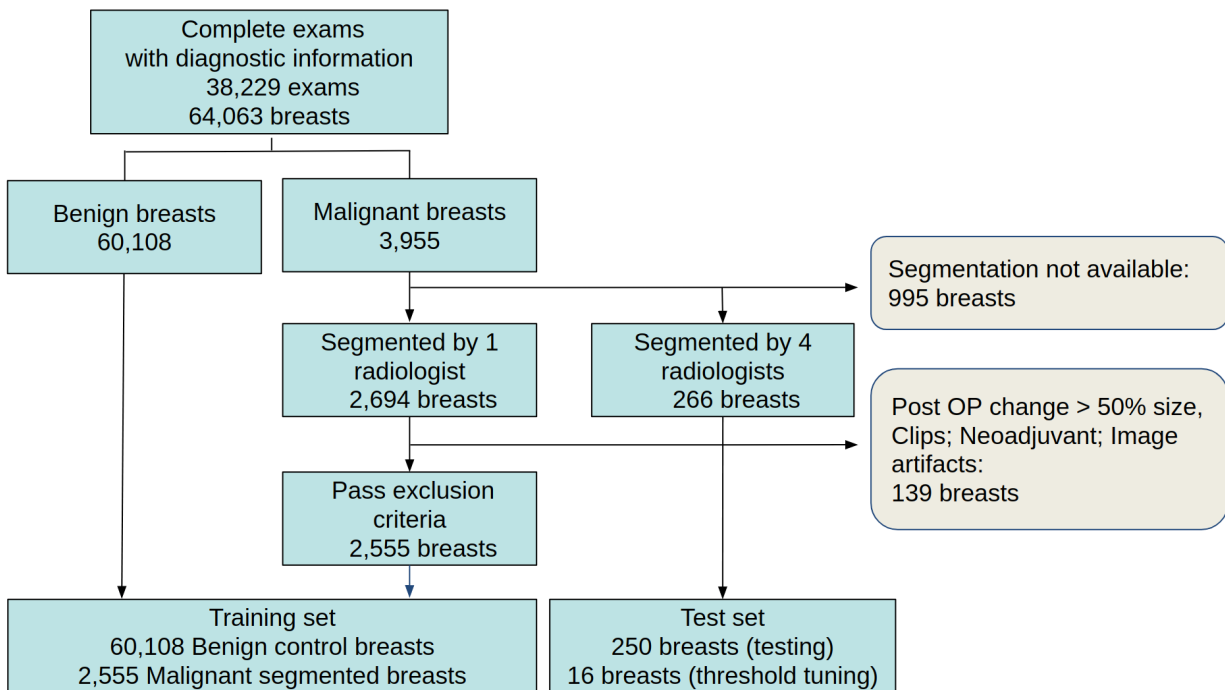


**Figure 1: Number of exams and breasts used in training and testing.** See also Table S1.

### Data Description and Harmonization

All breast MRI examinations were acquired on either a 1.5 or 3.0 Tesla GE scanner (GE Medical Systems, Waukesha, WI). Exams were acquired in the sagittal plane (Fig. 2A) at varying in-plane resolutions (Fig. 2B), 2–4 mm slice thickness, and varying repetition times (TR) and echo times (TE). Each MRI exam contained T1, T2, and a variable number ( $N = 3–8$ ) of T1 post-contrast images (T1c) sampled with varying time intervals. All images used fat saturation. In-plane sagittal resolution was harmonized by upsampling relatively low resolution images by a factor of two (Fig. 2B). Images intensity from different scanners were harmonized by dividing with the 95th percentile of pre-contrast T1 intensity. To summarize the dynamic contrast enhancement (DCE) we measure the volume transfer constant for the initial uptake and subsequent washout, DCE-in and DCE-out respectively (Fig 2A; DCE-in is the first post-contrast minus pre-contrast image; DCE-out is the intensity slope of all post-contrast images). Data collection, preprocessing and harmonization are described in more detail in the Supplement.

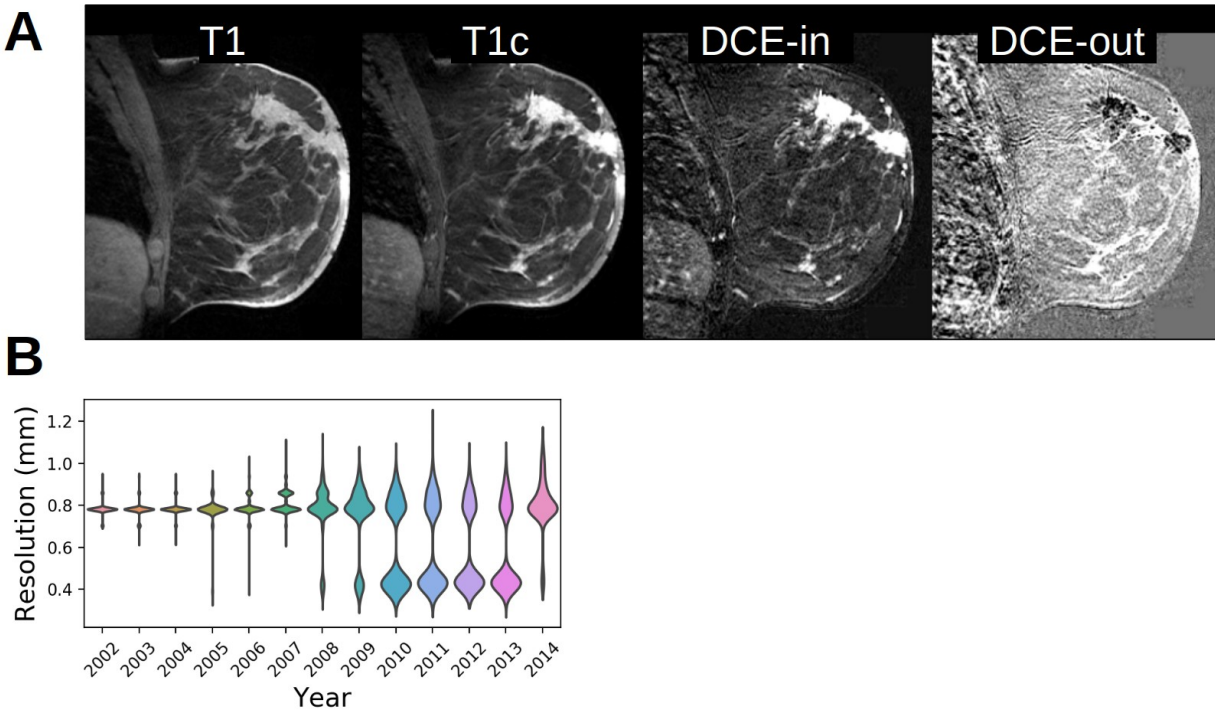


**Figure 2. A:** Example of pre- and first post-contrast images, T1 and T1c, respectively. Initial dynamic contrast enhancement in this tumor-positive case is evident after subtraction of the aligned T1c and T1 images (DCE-in). Subsequent washout (DCE-out) is evident in the subsequent contrast slope. **B:** T1c scans accrue over the years with a range of in-plane resolutions.

### Radiologist Segmentations

All segmentations were performed in 2D slices by dedicated breast radiologists (R1–R10, years of experience: 5, 8, 5, 5, 8, 12, 7, 13, 5, 2) using exams where cancer was proven through a biopsy. To train the network, 2,694 breasts were segmented by individual radiologists (R1–R10). These segmentations were subsequently reviewed by R1–R5 to ensure they met the inclusion criteria, resulting in 2,555 segmentations used for training (Fig. 1 and Table S1). To evaluate machine and human performance on independent test data an additional 266 breast cancers were independently segmented by all four radiologists (R1–R4). The common 2D slice to be segmented was selected by R5, containing the largest area of the index cancer. Radiologists performed segmentations on the T1c image, with the T1 and fat-saturated T2-weighted images available for reference. For the test data, we also provided the T1c-T1 subtraction (DCE-in) which quantifies initial uptake. See the Supplement for more details.

### Convolutional Neural Networks

We used networks based on the DeepMedic network (28) and a 3D U-Net (21), which have been used extensively for medical segmentation, including breast segmentation (20–25). The architecture of the 3D U-Net is described in Fig. 3 (Fig. S3 for the DeepMedic). Following previous studies (29) the traditional space-invariant implementation has been augmented by adding a spatial prior as input to the final classification. For the U-Net, the spatial prior was a breast mask, as in previous studies (21). This breast mask was computed using a separate U-Net operating on the entire image at lower resolution. This network was trained on a smaller number of manually segmented breast slices (N = 100; performed by the first author). To avoid blocking artifacts that are often observed in U-Nets (30) carefully re-designed the conventional

downsampling and upsampling steps. The 3D U-Net had approximately three million parameters. Details of the architectures, sampling, and training of the network parameters are in the Supplement (Fig. S3, S4).

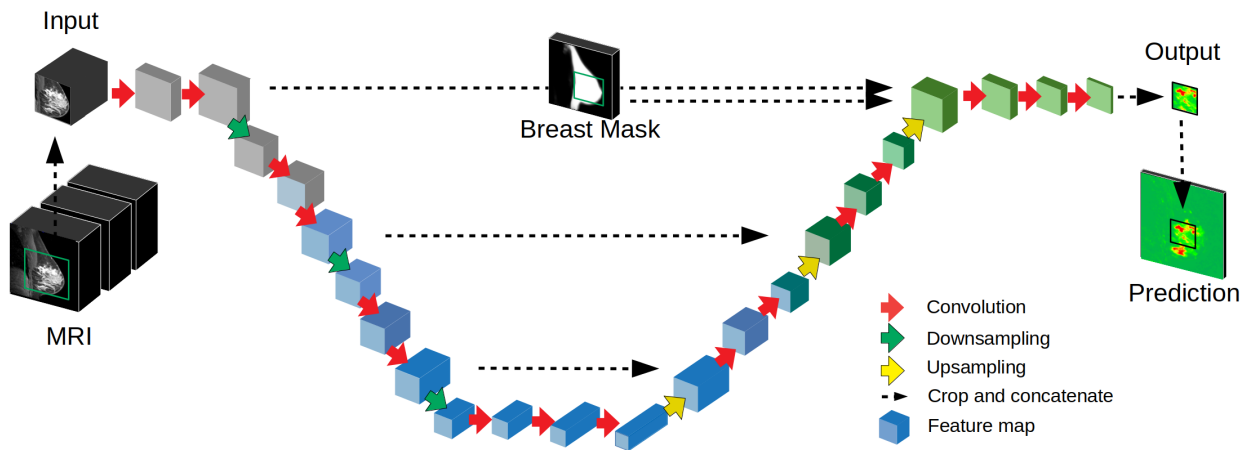


**Figure 3: Deep convolutional network used for segmentation.** We used a 3D U-Net with a total of 16 convolutional layers (orange arrows) resulting in 3D feature maps (blue blocks). The input MRI includes several modalities (see Fig. 2A). The network output is a prediction for a 2D sagittal slice, with probabilities for malignancy for each voxel (green/red map). The full volume is processed in non-overlapping image patches (green square on 'Input MRI'). A breast mask provides a spatial prior as input to the U-Net.

### Primary Outcome Measure

The network estimates for each voxel the probability of malignancy (Fig. 4). A binary segmentation was obtained by thresholding this probability at a fraction of the maximum in the selected slice (Fig. 4) and dismissing disconnected areas that did not reach the maximum. The primary outcome measure was the conventional Dice score (31) with a consensus segmentation as reference (e.g. Fig. 4; and Supplement for detail). A Dice score of 1.0 corresponds to perfect overlap and a score of 0.0 indicates no overlap.

### Statistical Methods:

All pairwise performance comparisons among different network architectures and between the network and radiologists used the Wilcoxon signed-rank test on the Dice score. We tested for equivalence in the Dice score of human and machine using TOST procedure (32). In this procedure performance is compared to bottom and top equivalence bounds, for which we selected the bottom and top performing radiologists. The comparisons were paired for the same exams, and we again performed a Wilcoxon signed-rank test.

## Results:

To select the preferred network architecture, input modalities, and harmonization method we trained various architectures (as described in the Supplement). We evaluated performance on a validation set, i.e. a fraction of the training data that is left out from training. Based on these results (Fig. S5) we selected a volumetric implementation of a 3D U-Net (Fig 3), which takes as inputs the first post contrast T1 (T1c), the initial uptake (T1c – T1), and the slope of the

subsequent contrast (T1c-slope) (Fig. 2A). These sagittal images were aligned with deformable co-registration (33) covering the volume of a single breast. Intensity was harmonized by scaling each exam separately with a robust maximum of the pre-contrast T1. When training this network on a dataset of different sizes we confirm the main hypothesis that the larger dataset significantly improves Dice score performance (0.63 for 240/240, 0.69 for 2,400/2,400, and 0.73 for 2,455/60,108 malignant/benign scans respectively evaluated on a validation set of 100 malignant scans; Fig. S6).

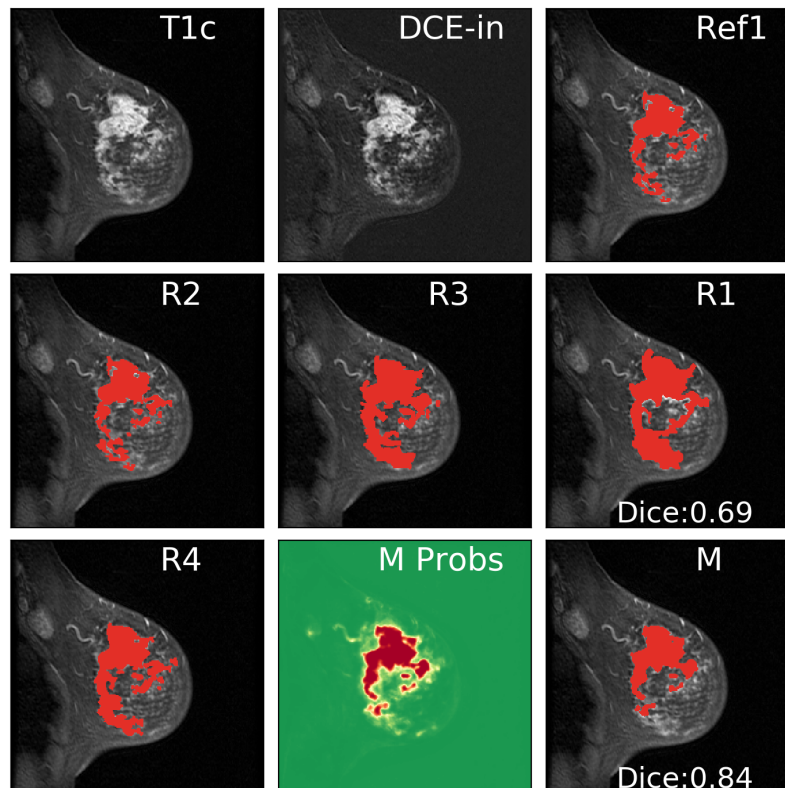


**Figure 4: Manual and automated segmentations of breast lesions. R1-R4:** Example segmentation of all four radiologists for a given slice, **T1c:** first post-contrast, **DCE-in:** T1c-T1 subtraction, **Ref1:** intersection of R2–R4 which serves as unbiased reference for R1, **M Probs:** output of the network indicating probability that a voxel is a tumor (green = low; red = high). **M:** model segmentation created by thresholding these probabilities. Dice scores here are computed using Ref1.

Performance of this final design was tested on an independent test of 266 malignant cases. Tumors were segmented independently by four breast radiologists (R1–R4) in a single 2D slice (Fig. 4). An unbiased reference segmentation was obtained for each radiologist using segmentations from the three remaining radiologists (e.g., Ref1 is the intersection of the segmentations of R2–R4 and is used to evaluate R1; Fig. 4). With this reference, we computed the receiver operating characteristic (ROC) curves (Fig. 5A for R1; Fig. S7A for R2–R4). The area under the ROC curve (AUC) is 0.996 when averaged over all 266 exams and the four references. The optimal threshold for converting continuous probabilities at the output of the network into binary segmentations was estimated using 16 exams of the test set (selected at random; Fig S7B). The Dice score of the remaining 250 exams of the test set (averaged over the four references) had a 5<sup>th</sup>–95<sup>th</sup> percentile range of 0.43–0.90 for the radiologists and 0.21–0.92 for the network (Fig. 5B). These mean Dice scores did not differ significantly between the network and the radiologists ( $W=14034$ ;  $p=0.15$ ,  $N=250$ ). The median Dice scores of the network were 0.76, 0.76, 0.77, and 0.76, and for the radiologists the median Dice scores were

0.69, 0.84, 0.78, and 0.84, with one value for each of the four references. To test for equivalence, we performed the TOST procedure (32) with radiologists performance as the lower and upper bounds for equivalence (R1 and R4, respectively; Fig. 5C). The Dice score of the network is significantly higher than that of R1 ( $W=9480$ ;  $p=5e-8$ ,  $N=250$ ) and lower than that of R4 ( $W=11763$ ;  $p=6e-4$ ,  $N=250$ ). In total, the mean performances of the network and the radiologists were indistinguishable, and median performance of the network was equivalent to that of the radiologists.

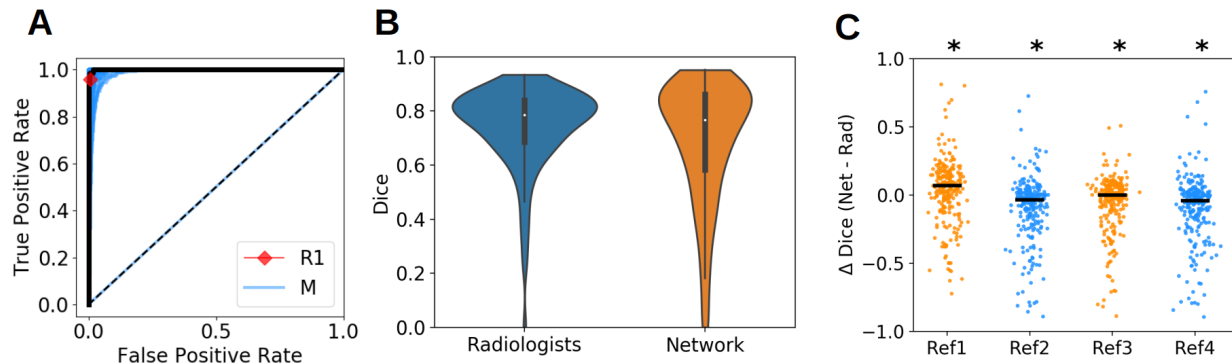


**Figure 5: Network and radiologist performance on test set.** **A:** ROC curves of the segmentation network for all exams (blue) and performance of radiologist R1 (diamond) with the intersection of R2–R4 as reference segmentation. The average ROC curve (black) had an AUC = 0.998. **B:** Distribution of Dice scores in 250 test cases averaged across four references did not differ between radiologists and the network (medians 0.79 and 0.77, respectively; Wilcoxon  $W=14034$ ,  $p=0.15$ ,  $N=250$ ). **C:** Difference in Dice score between the network and each radiologist ( $\Delta$  Dice) for each of the four reference segmentations. Each point represents one of the 250 test exams. The median Dice is higher for the network for Ref1 and Ref3 (orange) and higher for the radiologist for Ref2 and Ref4 (blue). (\*: Wilcoxon  $p < 0.05$ ).

There are several exams in which the network outperforms the average of the three radiologists ( $\Delta$  Dice  $> 0$ , Fig. 5C; see Fig. 4 for an example). But in several instances, the network performs worse than the radiologists ( $\Delta$  Dice  $< 0$ , Fig. 5C; see Fig. 6 for examples). The network deviates from the reference radiologist either in terms of the areas that it selected (Fig. 6A) or the tumor exact boundary (Fig. 6B). Network performance differed among tumor types (Fig. S8A), and was somewhat worse in the presence of prominent BPE (Fig. S8B).



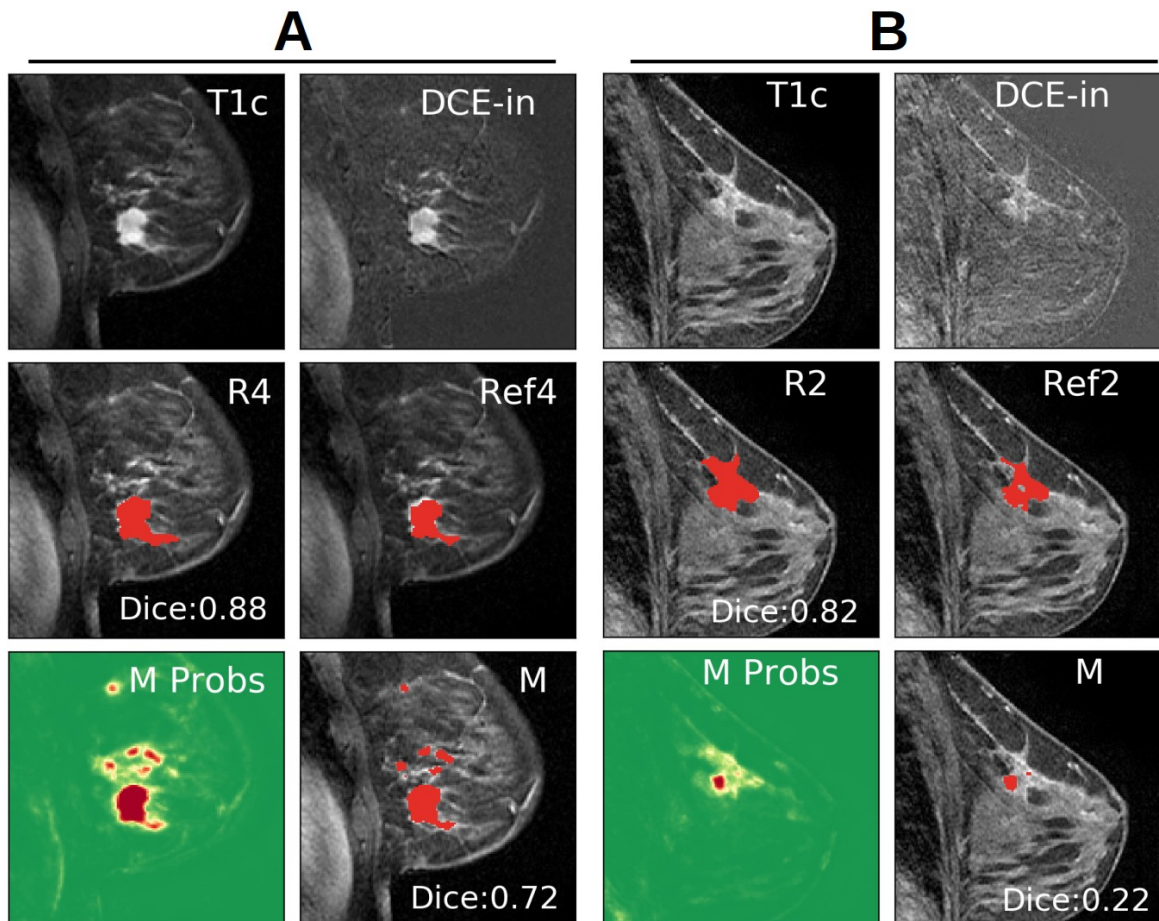


**Figure 6: Examples of cases in which the network deviates from the segmentation of the reference radiologist.** **A:** The network captures additional areas not selected by the radiologist R4. Dice score here shown for Ref4 (intersection of R1–R3). **B:** The network output (M Probs) captures the correct area, but after thresholding, low probability values yield a smaller region compared to the consensus segmentation (Ref2).

## Discussion

We demonstrated radiologist-level performance in automated segmentation of breast tumor lesions in MRI by optimizing the architecture of deep convolutional networks using a large training dataset of MRI scans, which consisted of 2,555 malignant and 60,108 benign breasts. This dataset is substantially larger than previous efforts with deep networks, which used only 50–250 MRI exams (20–25).

We obtained the best performance with a volumetric U-Net that is conceptually simpler than previous networks (21,22,24). Complex structures with fewer parameters may have been necessary to compensate for the smaller data-set sizes used in these earlier studies. For instance, Zhang et al. combined three different 2D U-Nets in a hierarchical manner (21); one network generated a breast mask, the second produced segmentations of tumors, and the third refined these segmentations. We used a similar approach at first, following the MultiPrior network (29) with a breast mask as a spatial prior, and a conditional random field (CRF) for post-processing. However, we found that a simpler 3D U-Net without these additional modules

sufficed. The U-Net also outperformed a DeepMedic (28), which we believe is the result of better integration of information at multiple spatial scales. Chen et al. used 2D U-Nets with a long-short-term-memory (LSTM) network at the input to process the contrast dynamic (22). Instead, we summarized the DCE in two images, capturing the initial contrast uptake and subsequent wash-out. This allowed us to harmonize the differing sampling intervals and the number of post-contrast images. Adoui et al. uses a Seg-Net which communicates only location information through residual connections. (24). This reduces the number of parameters as compared to a U-Net, and therefore may have required fewer training images. Other previous network methods cope with smaller training sets using pre-selected features (20), unsupervised clustering algorithm (25), or by leveraging shape priors (23).

Our final U-Net implementation differs from previous approaches in two important ways. First, we used a full 3D network instead of a conventional 2D network that processes individual slices independently (13,22,24–26). While this increased the number of network parameters, it also captured volumetric features missed in 2D processing. Our implementation also avoids sampling artifacts encountered in conventional implementations of U-Nets (30). While we did this with an apparent increase in complexity, our approach obviates the need of less carefully designed architectures to “unlearn” sampling errors.

Previous efforts to apply machine learning to breast lesion segmentation report Dice scores in the range of 0.60–0.77 (20–24), but the performance of these models has generally not been compared to that of trained radiologists. In a head-to-head comparison, Zhang et al. (21) reported a Dice score of  $0.72 \pm 0.28$  for the network and  $0.78 \pm 0.30$  for the radiologists. In the present study, automated segmentations matched the detailed segmentations of a trained radiologist with a Dice score of 0.77. Importantly, in the same dataset, we show statistical equivalence to radiologist performance in the range of 0.72–0.84. We note that the test set here includes difficult cases with small subcentimeter cancers, multicentric cancer and include patients with breast implants, all of which have often been excluded from previous studies. Our study is retrospective and limited to a single institution. However, the data set is heterogeneous having been collected over 12 years from different scanner types, magnet strengths (1.5 and 3.0 Tesla), different breast coils, which results in variable spatial and temporal resolutions. All these factors together add to the difficulty and clinical realism of this study

The network classifies each voxel in the image and thus in principle provides volumetric segmentation. The main clinical utility is to facilitate volumetric assessment, which is not broadly used despite proven benefit (1,3,4). It should be noted, however, that we evaluated automated segmentations only in 2D slices. Another limitation of the work is that we used sagittal images, which was standard practice at our institution until 2014, and which therefore characterized most of the historical data. Breast MRI protocols are often acquired in the axial plane and with continued improvements in technology, with higher temporal and spatial resolution. Thus, future studies should focus on volumetric evaluation of segmentations based on high-resolution multi-planar breast MRI. To facilitate such studies we make all code and the pretrained network freely available on github.

In the clinic, radiologist-level performance in automated segmentation has the potential to aid detection and diagnosis and improve overall workflow of radiologists. In research, fast and accurate tumor segmentations might help identify important prognostic and predictive biomarkers and improve our understanding of breast cancer.

# References (35 max)

1. Partridge SC, Gibbs JE, Lu Y, et al. MRI measurements of breast tumor volume predict response to neoadjuvant chemotherapy and recurrence-free survival. *AJR Am J Roentgenol.* 2005;184(6):1774–1781.
2. Bhooshan N, Giger ML, Jansen SA, Li H, Lan L, Newstead GM. Cancerous Breast Lesions on Dynamic Contrast-enhanced MR Images: Computerized Characterization for Image-based Prognostic Markers. *Radiology.* 2010;254(3):680–690.
3. Hylton NM, Gatsonis CA, Rosen MA, et al. Neoadjuvant Chemotherapy for Breast Cancer: Functional Tumor Volume by MR Imaging Predicts Recurrence-free Survival-Results from the ACRIN 6657/CALGB 150007 I-SPY 1 TRIAL. *Radiology.* 2016;279(1):44–55.
4. Drukker K, Li H, Antropova N, Edwards A, Papaioannou J, Giger ML. Most-enhancing tumor volume by MRI radiomics predicts recurrence-free survival “early on” in neoadjuvant treatment of breast cancer. *Cancer Imaging.* 2018;18.
5. de Moor T, Rodriguez-Ruiz A, Mérida AG, Mann R, Teuwen J. Automated soft tissue lesion detection and segmentation in digital mammography using a u-net deep learning network. *ArXiv180206865 Cs.* 2018
6. Kallenberg M, Petersen K, Nielsen M, et al. Unsupervised Deep Learning Applied to Breast Density Segmentation and Mammographic Risk Scoring. *IEEE Trans Med Imaging.* 2016;35(5):1322–1331.
7. Dhungel N, Carneiro G, Bradley A. The Automated Learning of Deep Features for Breast Mass Classification from Mammograms. 2016. p. 106–114.
8. Dhungel N, Carneiro G, Bradley AP. Automated Mass Detection in Mammograms Using Cascaded Deep Learning and Random Forests. 2015 Int Conf Digit Image Comput Tech Appl DICTA. 2015. p. 1–8.
9. Kooi T, Litjens G, van Ginneken B, et al. Large scale deep learning for computer aided detection of mammographic lesions. *Med Image Anal.* 2017;35:303–312.
10. Becker AS, Marcon M, Ghafoor S, Wurnig MC, Frauenfelder T, Boss A. Deep Learning in Mammography: Diagnostic Accuracy of a Multipurpose Image Analysis Software in the Detection of Breast Cancer. *Invest Radiol.* 2017;52(7):434–440.
11. Zhu W, Lou Q, Vang YS, Xie X. Deep Multi-instance Networks with Sparse Label Assignment for Whole Mammogram Classification. *ArXiv161205968 Cs.* 2016
12. Ribli D, Horváth A, Unger Z, Pollner P, Csabai I. Detecting and classifying lesions in mammograms with Deep Learning. *Sci Rep.* 2018;8(1):1–7.
13. Wu N, Phang J, Park J, et al. Deep Neural Networks Improve Radiologists’ Performance in Breast Cancer Screening. *IEEE Trans Med Imaging.* 2019;
14. McKinney SM, Sieniek M, Godbole V, et al. International evaluation of an AI system for breast cancer screening. *Nature.* 2020;577(7788):89–94.
15. Warner E, Plewes DB, Hill KA, et al. Surveillance of BRCA1 and BRCA2 mutation carriers with magnetic resonance imaging, ultrasound, mammography, and clinical breast examination. *JAMA.* 2004;292(11):1317–1325.
16. Lehman CD, Isaacs C, Schnall MD, et al. Cancer yield of mammography, MR, and US in high-risk women: prospective multi-institution breast cancer screening study. *Radiology.* 2007;244(2):381–388.
17. Chiarelli AM, Prummel MV, Muradali D, et al. Effectiveness of screening with annual magnetic resonance imaging and mammography: results of the initial screen from the ontario high risk breast screening program. *J Clin Oncol Off J Am Soc Clin Oncol.* 2014;32(21):2224–2230.
18. Marinovich ML, Houssami N, Macaskill P, et al. Meta-Analysis of Magnetic Resonance

- Imaging in Detecting Residual Breast Cancer After Neoadjuvant Therapy. *JNCI J Natl Cancer Inst. Oxford Academic*; 2013;105(5):321–333.
19. Dontchos BN, Rahbar H, Partridge SC, et al. Are Qualitative Assessments of Background Parenchymal Enhancement, Amount of Fibroglandular Tissue on MR Images, and Mammographic Density Associated with Breast Cancer Risk? *Radiology*. 2015;276(2):371–380.
  20. Wu H, Gallego-Ortiz C, Martel A. Deep Artificial Neural Network Approach to Automated Lesion Segmentation in Breast. *Proc 3rd MICCAI Workshop Breast Image Anal 2015. Munich, Germany*; 2015. p. 73–80.
  21. Zhang J, Saha A, Zhu Z, Mazurowski MA. Hierarchical Convolutional Neural Networks for Segmentation of Breast Tumors in MRI With Application to Radiogenomics. *IEEE Trans Med Imaging*. 2019;38(2):435–447.
  22. Chen M, Zheng H, Lu C, Tu E, Yang J, Kasabov N. A Spatio-Temporal Fully Convolutional Network for Breast Lesion Segmentation in DCE-MRI. In: Cheng L, Leung ACS, Ozawa S, editors. *Neural Inf Process. Cham: Springer International Publishing*; 2018. p. 358–368.
  23. Maicas G, Carneiro G, Bradley AP. Globally optimal breast mass segmentation from DCE-MRI using deep semantic segmentation as shape prior. *2017 IEEE 14th Int Symp Biomed Imaging ISBI 2017. Melbourne, Australia: IEEE*; 2017. p. 305–309
  24. Adoui, Mahmoudi, Larhman, Benjelloun. MRI Breast Tumor Segmentation Using Different Encoder and Decoder CNN Architectures. *Computers*. 2019;8(3):52.
  25. Parekh VS, Macura KJ, Harvey S, et al. Multiparametric Deep Learning Tissue Signatures for a Radiological Biomarker of Breast Cancer: Preliminary Results. *Med Phys*. 2020;47(1):75–88.
  26. Spuhler KD, Ding J, Liu C, et al. Task-based assessment of a convolutional neural network for segmenting breast lesions for radiomic analysis. *Magn Reson Med*. 2019;82(2):786.
  27. Monticciolo DL, Newell MS, Moy L, Niell B, Monsees B, Sickles EA. Breast Cancer Screening in Women at Higher-Than-Average Risk: Recommendations From the ACR. *J Am Coll Radiol*. 2018;15(3):408–414
  28. Kamnitsas K, Ledig C, Newcombe VFJ, et al. Efficient multi-scale 3D CNN with fully connected CRF for accurate brain lesion segmentation. *Med Image Anal*. 2017;36:61–78.
  29. Hirsch L, Huang Y, Parra LC. Segmentation of lesioned brain anatomy with deep volumetric neural networks and multiple spatial priors achieves human-level performance. *ArXiv190510010 Cs Eess Q-Bio Stat*. 2019
  30. Aitken A, Ledig C, Theis L, Caballero J, Wang Z, Shi W. Checkerboard artifact free sub-pixel convolution: A note on sub-pixel convolution, resize convolution and convolution resize. *ArXiv170702937 Cs*. 2017
  31. Dice LR. Measures of the Amount of Ecologic Association Between Species. *Ecology*. 1945;26(3):297–302.
  32. Walker E, Nowacki AS. Understanding equivalence and noninferiority testing. *J Gen Intern Med*. 2011;26(2):192–196.
  33. Rueckert D, Sonoda LI, Hayes C, Hill DLG, Leach MO, Hawkes DJ. Nonrigid registration using free-form deformations: application to breast MR images. *IEEE Trans Med Imaging*. 1999;18(8):712–721.
  34. Wrobel J, Martin M, Bakshi R, et al. Intensity warping for multisite MRI harmonization. *Neuroscience*; 2019 Jun
  35. Kingma DP, Ba J. Adam: A Method for Stochastic Optimization. *ArXiv14126980 Cs*. 2017

## Supplementary Material

MRI exams	38,229
Scanned breasts	64,063
Biopsy-proven cancer	3,955
Benign breasts used for training	60,108
Malignant breasts used for training	2,555 × 1 radiologist
Malignant breasts used for testing	266 × 4 radiologists (250 for testing, 16 for threshold tuning)

**Table S1: Summary of available data used in training and testing.**

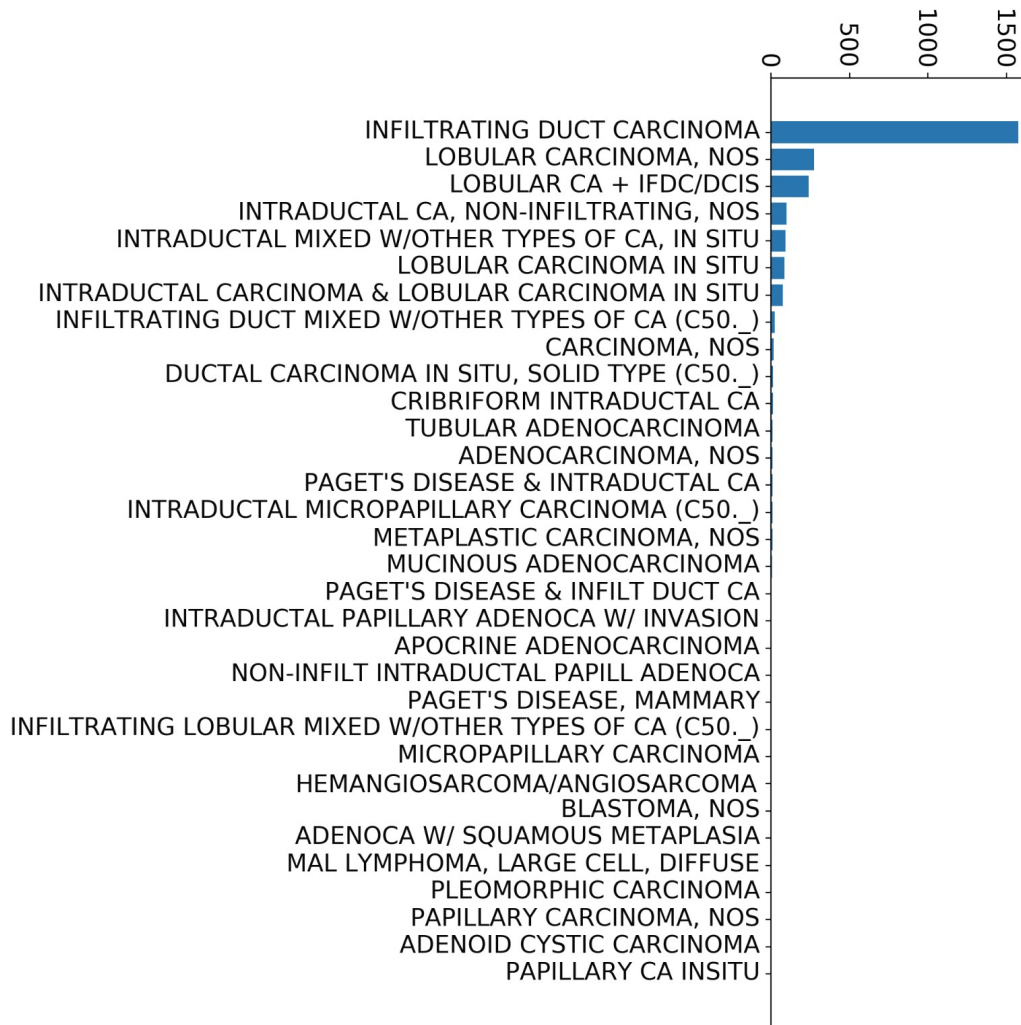


**Figure S1: Number of tumors in the overall dataset.**

## Data Description and Preprocessing

All breast MRI examination data were acquired with GE MRI scanners (GE Medical Systems, Waukesha, WI) with either a 1.5 or 3.0 Tesla fields and dedicated 4, 7, 8, or 16-channel breast coils. Five different scanner types were used: Signa Excite, Genesis Signa, Discovery, Signa HDxt and Optima MR450w. Exams were acquired in the sagittal plane (Fig. 2A) at various in-plane resolutions (Fig. 2B), 2–4 mm lateral resolutions, and varying TR and TE times. Intravenous gadolinium-based contrast agent was administered at 0.10 mmol per kg of body weight and at a rate of 2 ml/sec. Prior to analysis, data were de-identified by removing all patient information and by saving exams with anonymized patient identifiers. DICOM headers were used to identify the modality (T1 or T2), laterality (left or right breast), fat saturation, and acquisition time for pre- and post-contrast T1 images. In total, data was available for 38,229 exams with complete imaging and diagnostic information for 64,063 breasts (not all exams included two breasts).

## Harmonization

To compensate for the diversity of data acquisition techniques in the 12-year period in which the study data was collected, it was necessary to harmonize the spatial resolution, intensity, and contrast dynamics of the data. In-plane sagittal resolution was harmonized by upsampling low resolution images by a factor of two to approximately match higher resolution images (using the resize function in Python package scikit-image) (Fig 2B). Lateral resolution was left unchanged. Images from different scanners were harmonized by using intensity normalization, similar previous work (34). For this purpose, a breast mask was established for each T1 image (see below). Then, for each scanner, we computed a histogram of all breast voxels and calculated a nonlinear transformation to transform these histograms into a standard distribution (Fig. S2). We deviate from (34) by using a Chi-square of degree  $k=4$  as target distribution. This transformation was then applied to all image intensities of that scanner, including pre- and post-contrast images. We also used an intensity harmonization based on each exam by dividing all images from an exam with the 95th percentile of the pre-contrast T1 intensity. This simpler exam-based alternative was ultimately adopted as it outperformed the scanner-based intensity harmonization (see Fig. S5D below). Finally, to harmonize the contrast dynamic, we computed the initial uptake (DCE-in) and the intensity slope over time of the post-contrast MRIs to capture DCE wash-out (DCE-out) measured in units of  $\text{min}^{-1}$ , i.e. volume transfer constants (Fig.2A). This initial uptake and subsequent slope were computed after deformable co-registration with NiftyReg (33), where we used the first post-contrast image T1c as a common reference for all images.

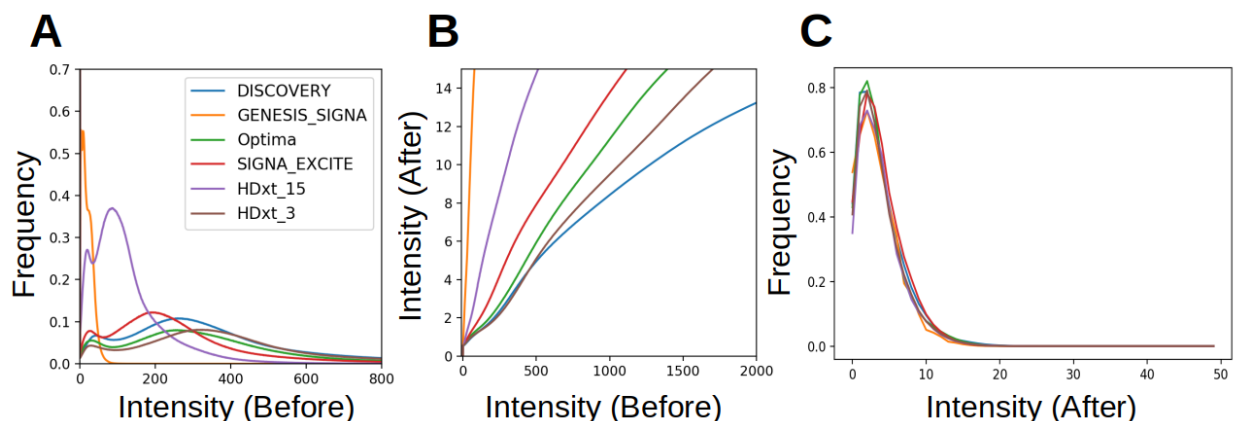


**Figure S2.** Intensity harmonization across different scanners to a standard Chi-square distribution: **A:** Intensity distribution of each scanner and B-field intensity (each distribution belongs to one of a total of six scanner manufacturers identified). **B:** Non-linear transformation mapping the intensities from each scanner to intensities of a target distribution (same colors as in panel A). **C:** Intensities distribution after the non-linear mapping transformation. They all approximate the target of a Chi-square distribution (with  $k=4$ ).

## Radiologist Segmentations

From the available 3,955 confirmed malignant exams 2,694 exams were selected at random (Fig.1). Selected exams included all required sequences (T1, T1c, and T2), were of adequate image quality, and were free from gross imaging artifacts. Of these 2,694 exams, radiologists R5–R8 segmented an initial 880 exams, whereby segmentation was limited to the largest index cancer. Radiologists R1–R4 segmented an additional 1,814 exams, whereby segmentation included the entire extent of disease included in the 2D slice to provide the network a more complete sample of tumor voxels. Note that benign voxels for training are taken only from benign breasts, so that segmentations performed by R5–R8 on the largest index cancer can still be used for training.

All breast cancer segmentations were reviewed by radiologists R1–R5 and exams were excluded in any of the following circumstances: significant post-surgical change with partial resection of the cancer, post-biopsy change larger than 50% of the index cancer, MRI performed of breast cancer after having been treated with neoadjuvant chemotherapy, and inaccurate segmentation that was missing more than 50% of the mass. Of the 2,694 exams, 139 were excluded resulting in a total of 2,555 segmented breast cancer exams, which were used for network training.

To evaluate machine and human performance on an independent test set, an additional 266 confirmed-malignant exams were selected at random with the same inclusion/exclusion criteria. Each of these 266 tumors were segmented by all four radiologists (R1–R4), with the single 2D slice having already been selected by R5. These segmentations included the entire extent of the disease.

Because most patients had multiple screening breast MRI, the dataset contains multiple scans of the same breast at different time points. After selecting the training/validation/testing partitions, any breasts that overlapped between them were removed from the training set.

Radiologists performed segmentations on the first post-contrast image (T1c) with the pre-contrast T1 and T2 images available for reference, along with the existing radiology reports. For the test data, we also provided the initial uptake image (DCE-in). Segmentations were performed with a custom graphic user interface (based on the Tkinter Python toolbox) using a tablet or mouse (based on personal preference).

The Dice score was used for evaluation of the segmentation generated by the network against the radiologist's segmentation. This metric is common in segmentation tasks (21,29), and is defined as:  $Dice = 2TP / (2TP + FP + FN)$  where TP = true positives, FN = false negatives, and FP = false positives, corresponding to classified voxels against the defined reference.

## Implementation Detail for DeepMedic

The DeepMedic network follows the implementation of Hirsch et al. (29) and was based on the architecture proposed in Kamnitsas et al. (28). The general architecture is shown in Fig. S3.



The network consists of a 3D convolutional neural network (CNN) with 11 layers and two parallel pathways. All layers contain learnable kernels (size  $3 \times 3 \times 3$ ) and ReLU as nonlinear activation functions, except the last classification layer, which has a Softmax activation function. During training, this network takes as input a patch of  $13 \times 35 \times 35$  voxels around a target patch of  $9 \times 9$  to be classified and a larger field-of-view of  $13 \times 75 \times 75$  voxels at half-resolution for extracting contextual features. As with the 3D U-Net, we add a TPM to provide prior spatial information. Here the TPM was the average segmentation of the lesions in the training data for all breasts after rigid body registration. Prior probabilities for the target patch are extracted from a TPM and added as input to the final classification. This TPM is constructed by averaging the segmentations from the training set. The final three layers take the concatenated output of all three pathways as input and classify the target patch with fully connected layers and no additional spatial mixing (kernel size  $1 \times 1 \times 1$ ). In total, the DeepMedic network had approximately one million parameters.

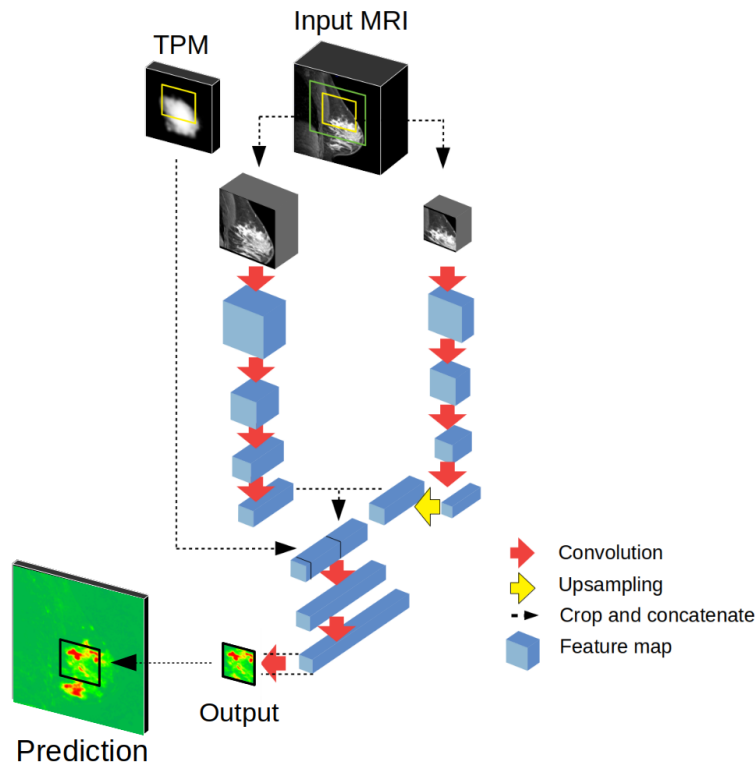


**Figure S3:** The DeepMedic network processes an image section or patch at high-resolution (contoured in yellow) and in parallel a larger patch (contoured in green) at half the original resolution. The output is a 2D image patch, with probability predictions per pixel for the center of the input image volume. A Tissue Probability Map (TPM) is added as extra features, which was made from averaging tumor segmentations from the training set.

### Implementation Detail for 3D U-Net

The 3D U-Net also follows the implementation of Hirsch et al. (29). The U-Net is a 3D CNN with 16 layers. The input is an image patch of dimensions  $19 \times 75 \times 75$  at full resolution (see Fig. 3, orange square in input), which passes through all convolutional layers with

learnable kernels of size  $3 \times 3 \times 3$  and ReLU as nonlinear activation functions. The layers are organized in convolutional blocks, consisting each of two convolutional layers, one downsampling layer in the first half of the network, and upsampling layers in the second half of the network. Downsampling is performed with average pooling layers, and upsampling with transposed convolutional layers with fixed weights (see implementation of upsampling and downsampling in the U-Net). Residual connections concatenate the feature maps of each block on the same scale (see Fig. 3). The last layer has kernels of size  $1^3$  with a Softmax activation function, which outputs a prediction for the center  $37 \times 37$  area of the middle sagittal slice of the input (see Fig. 3, black square on prediction).

Implementation and training of the DeepMedic and the U-Net were performed in Python 2.7, with Keras 2.3.1 using TensorFlow backend 1.14.0, and NumPy version 1.16.6. Initialization of the kernel weights of the DeepMedic was done with Keras's Orthogonal initializer. The U-Net's kernel weights were initialized using Keras's default glorot uniform initializer. Both NumPy and TensorFlow were seeded with seed numbers 1 and 2, respectively, for initialization of all random numbers.

### **Implementation of Upsampling and Downsampling in the U-Net**

Conventional implementations of U-Net are prone to blocking artifacts (30). We carefully designed the downsampling and upsampling steps to avoid these artifacts. In all layers we selected "valid" padding, which reduced the size of the feature maps on each convolutional layer such that the model depth was kept relatively low at 4 downsampling blocks and 4 upsampling blocks. Downsampling was performed using average pooling with a kernel of size 3 and stride 2. Upsampling used a transposed convolution with fixed kernels of size 3, with fixed weights (0.5, 1, and 0.5) to perform exact bilinear interpolation. Residual connections between downsampling and upsampling pathways required cropping borders by 1 voxel to match feature map dimensions. We note that this implementation deviates from common implementations of the U-Net. Typically, U-Nets use average pooling with variable kernel sizes for downsampling and learnable weights in the transposed convolutional layers for upsampling, but this can cause border and checkerboard artifacts (30). Fixing the transpose convolution parameter, as we have done here, seems to limit the flexibility of the network while imposing additional processing steps; however, this is worthwhile to avoid blocking artifacts. Additionally, this reduces the number of trainable parameters and provides a better training starting point by ensuring artifact-free upsampling from the start.

### **Network Training**

The network is trained using conventional gradient descent to minimize a generalized Dice loss (29) using the Adam optimizer (35) (Fig. S4A and Fig. S4B). We used a batch of size 16 for each weight-updating iteration. The Dice score for the validation set was monitored at every epoch (Fig. S4C), which occurred every 2,976 weight update iterations with 48,000 image patches drawn from 4,800 scans per epoch. For data augmentation, each input was randomly rotated on one of three rotation axes. The learning rate was set to  $10^{-6}$ , and adapted automatically with the Adam optimizer (35). Learning was halted when we observed overtraining on the validation set, which is a subset of the training data not used for training (70 exams selected at random containing 42 malignant scans). During training, image patches were presented containing tumor and non-tumor regions in a ratio of 1:4, as the benign tissue samples available far outweighed the malignant tissue samples available. Tumor voxels were sampled uniformly across all segmented slices. Non-tumor voxels were sampled anywhere in

the benign scans, enriching for locations with high T1c values. This sampling process focused the training on the areas of the benign exams that are most challenging to classify due to BPE. No strong overfitting behavior was observed, so regularization was not applied, such as dropout or L2 penalty.

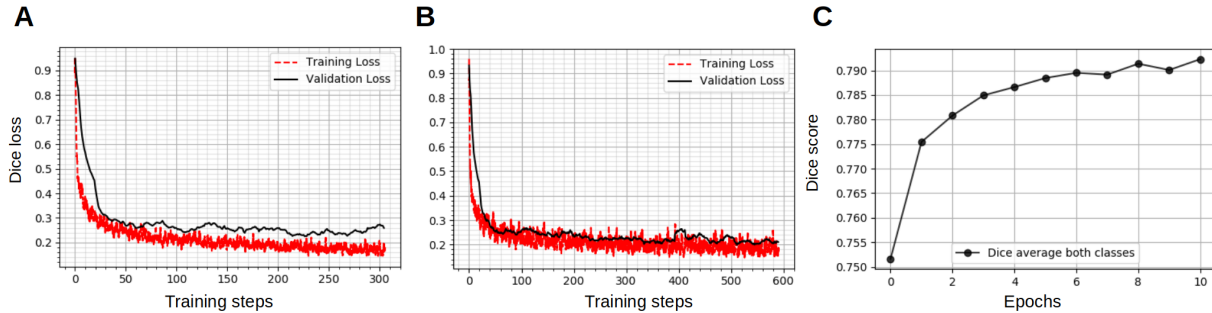


**Figure S4:** Training curves for the network. **A:** Training (red) and validation (black) loss during training on a set of 240 malignant and 240 benign breasts showing clear signs of overfitting (the loss keeps decreasing on the training data (red) but starts increasing on the validation data (black)). **B:** Training (red) and validation (black) set loss on the full training set (2,555 malignant and 60,108 benign breasts). Both losses decrease during training, showing asymptotic behavior and no overfitting. **C:** Average Dice score for both background and foreground voxels taken each epoch on the validation set containing 100 malignant scans. Each epoch consists of a full pass through all malignants in each set.

## Network Architecture Optimization

We organized the architecture optimization as a series of choices between alternative methods evaluated based on the Dice score of the validation set. In all comparisons that follow, we report the number of malignant exams used for training and validation ( $N_t$  and  $N_v$ , respectively), the median Dice score for the two methods on the validation set, and the p-value of a paired test on the difference of medians.

First, we used a MultiPrior network (29), which is a DeepMedic network (28) with additional prior information (Fig. 3A). Specifically, it included a TPM to provide spatial priors on likely location of tumors and a CRF to provide morphological spatial priors. Adding this TPM improved performance by removing erroneous malignant voxels outside the breast ( $N_t = 869$ ;  $N_v = 29$ ; median Dice without TPM: 0.64; median Dice with TPM: 0.71;  $W = 80.5$ ,  $p = 0.005$ ). In contrast, adding a CRF did not enhance performance (median Dice without CRF: 0.75; median Dice with CRF: 0.72;  $W = 420.0$ ,  $p = 0.69$ ,  $N = 42$ ), so we refrained from future use. This 3D CRF follows the structure of the MultiPrior model (29) implemented with a Gaussian filter and a bilateral filter, where we chose parameters for both filter widths (variance) to be 1, and the weight constant for both filters equal to 1, done with a simple grid search in the interval [0-5] on a small number of segmentations from the validation set. We then tested the U-Net with a TPM, where the TPM was a simple binary breast mask (Fig. 3). We found that the U-Net + TPM architecture outperformed the DeepMedic + TPM (Fig. S5A,  $N_t = 1025$ ;  $N_v = 20$ ; median Dice DeepMedic + TPM: 0.69; median Dice U-Net + TPM: 0.8;  $W = 26$ ,  $p = 0.003$ ). Next, we tested the U-Net without the use of the breast mask and found that performance was unchanged (Fig. S5B,  $N_t = 1025$ ;  $N_v = 20$ ; median Dice U-Net + TPM: 0.81; median Dice U-Net: 0.82;  $W = 113$ ,  $p = 0.93$ ). We tested whether addition of the T2 scans could improve performance, however, addition of

coregistered T2 images actually decreased Dice score performance on the validation set (Fig. S5C,  $N_t = 2,555$ ;  $N_v = 42$ ; median Dice without T2: 0.75; median Dice with T2: 0.67;  $W = 188.0$ ,  $p = 0.001$ ). Finally, we compared the nonlinear intensity harmonization procedure (as described in Fig. S2) with a normalization that scales intensity separately for each exam. We found no difference in performance (Fig. S5D,  $N_t = 2,555$ ;  $N_v = 42$ ; median Dice nonlinear intensity harmonization: 0.8; median Dice exam-based scaling: 0.81;  $W = 515$ ,  $p = 0.16$ ), so we adopted the simpler scaling technique. Adding the slope of the contrast dynamic after the first contrast image significantly improved performance after training for 6 epochs in a balanced set containing equal number of malignant and benign scans (Fig. S6E,  $N_t=2,400$ ;  $N_v=100$ , median Dice without slopes: 0.6, median Dice with slopes: 0.66;  $W=1836$ ,  $p=0.02$ ).

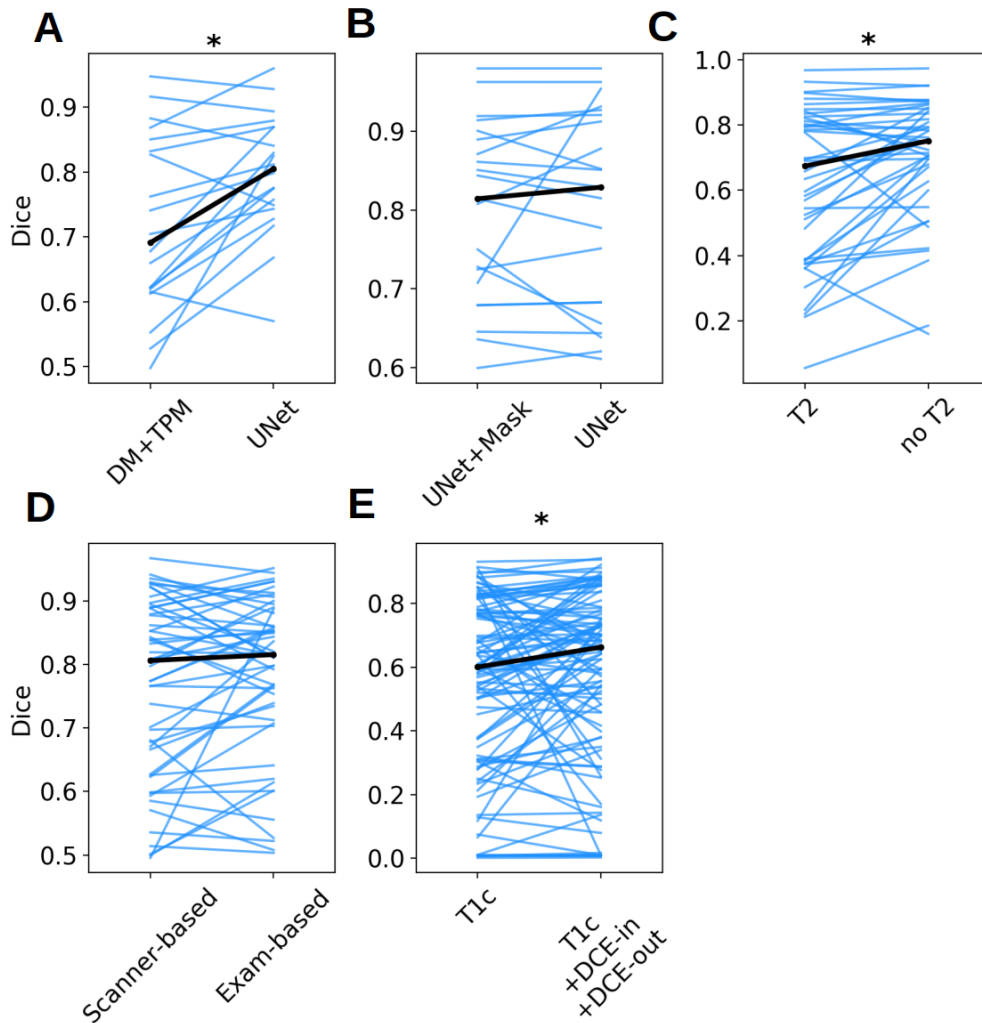


**Figure S5: Architecture optimization.** Pairwise comparison of five conditions for model selection. **A:** Architecture based on the DeepMedic adding spatial priors against the U-Net. **B:** The U-Net against a U-Net using spatial information on breast tissue location. **C:** Addition or exclusion of T2-weighted scans. **D:** Two different methods for harmonization of voxel intensities in the images, namely nonlinear transformation dependent on the scanner manufacturer (see Fig. S2) against a simpler scaling method based on the T1-weighted scan of each exam. **E:** Benefit of addition of contrast enhancement dynamics (DCE-in, DCE-out) (\* : Wilcoxon  $p < 0.05$ ).

## Training with different data set size

The basic hypothesis of this work is that training a deep network with a large dataset would significantly improve performance so as to reach radiologist-level performance. Performance gains with increased training set sizes are well established in machine learning. Nonetheless, we wanted to test this here explicitly for the typical dataset sizes used here and in the literature. When training this network on a typical dataset of 240 malignant and 240 benign scans the network achieved a Dice score of 0.63 on a fixed validation set (N=100, Figure S4). A tenfold larger training set with 2,400 malignant and 2,400 benign scans achieved a Dice score of 0.69 in the same fixed validation set. Finally the validation Dice score on the full data set with two order of magnitude more benign scans (2,455 malignant and 60,108 benigns) was of 0.73 (Figure S4). Both these gains in performance on a validation set were statistically significant (N=100, W=940,  $p=0.001$  small vs medium, N=100, W=1230,  $p=0.03$  medium vs large). Performance on this validation set (that is part of the training set) is lower than on the test set (compare with Fig. S6 with Fig. 4). The reason for this is that the test set contains more detailed segmentations necessary for multifocal lesions.

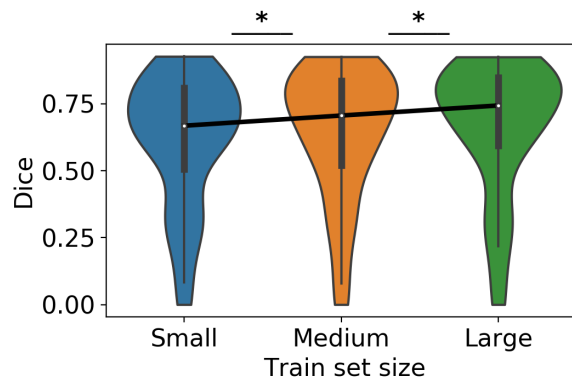
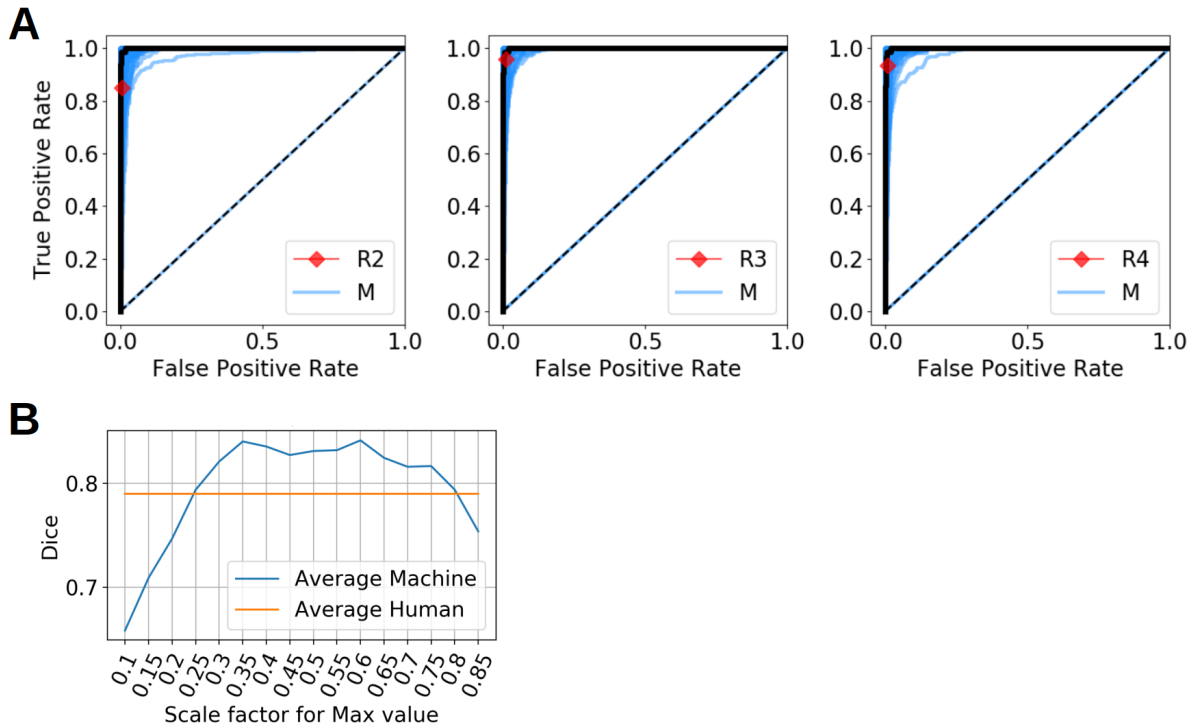


**Figure S6:** Performance comparison over three different training set sizes: Each of the sets has the same scans used for validation (100 malignants and 100 benigns) and testing (250 malignants), varying only the amount for training: The number of malignant/benign scans available in each set are: 240/240 in the small set, 2,400/2,400 for the medium set, and 2,455/60,108 in the large (complete) set. The median Dice score is 0.66, 0.69 and 0.73 respectively (\* indicates a pairwise significant difference between each group).

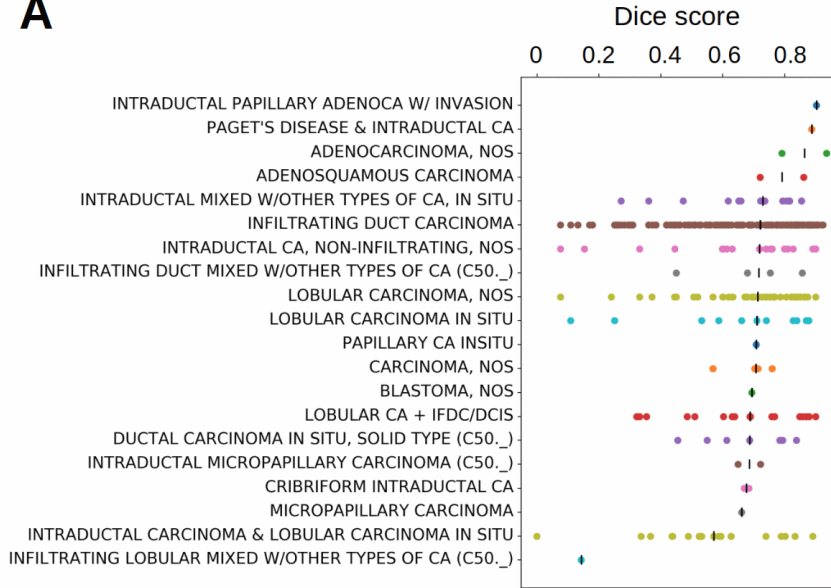
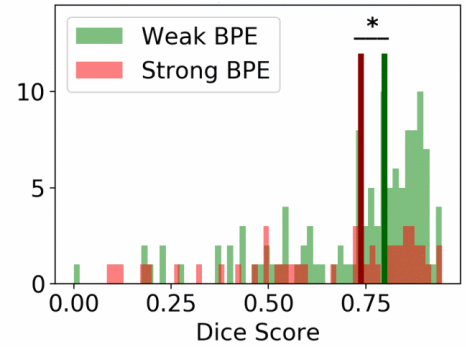
## Using a Consensus Segmentation as Reference

To evaluate the performance on the test set, we constructed a reference segmentation by combining the segmentations of multiple radiologists. To prevent bias, this consensus segmentation did not include the segmentation of the radiologist being evaluated. Thus, each of the four radiologists had a separate reference segmentation that excluded the segmentation of the radiologist being tested. We used the intersection to combine the segmentations of the three other radiologists, including only voxels on which all three agreed. The exact boundary of the tumor in the automated segmentation is dependent on the threshold applied to the output probabilities. ROC curves for different thresholds are shown in Figure 5A and Fig S7A. To select the best threshold we computed the Dice score at different thresholds averaged over the four references (Fig. S7B) on a small portion of the test data (N = 16) selected at random. The best threshold value in Figure S7B was 0.60. Note that this threshold is relative to the maximum value in a test slice as described in the Methods section (primary outcome measure). This

relative threshold implements the prior knowledge (available to both the machine and the radiologist) that the 2D slice contains a malignant lesion.



**Figure S7:** Network performance as a function of threshold of the network output. **A:** ROC curves for Ref2–Ref4 on 266 test cases (blue) and average ROC (black). Corresponding AUC were 0.996, 0.995, and 0.995, respectively. The performance of radiologists R2–R4 are shown as red diamonds. **B:** Dice score averaged over the four references and a subset of the test exams ( $N = 16$ ) for different threshold values.

**A****B**

**Figure S8: Segmentation performance of the network depends on BPE and type of tumor.**

**A:** For each tumor type, the performance of the model is displayed, and the median is marked with a black line (ANOVA,  $F = 2.12$ ,  $p = 0.004$ ,  $df = 262$ ). **B:** Histograms showing Dice scores for the network, depending on the strength of BPE as assessed in the radiology reports. Radiologist performance is not affected by breast density (not shown), whereas the model's performance decays in the presence of strong BPE (median Dice  $\leq 75\%$  BPE: 0.79; median Dice  $\geq 75\%$  BPE: 0.73;  $U = 2592$ ;  $p = 0.02$ , Mann Whitney-U).